A Modified Model and Algorithm for Flow-Enhanced Crystallization—Application to Fiber Spinning

Prashant Shrikhande,* William H. Kohler, Anthony J. McHugh

Department of Chemical Engineering, Lehigh University, Bethlehem, Pennsylvania 18015

Received 26 April 2005; accepted 26 August 2005
DOI 10.1002/app.23045
Published online in Wiley InterScience (www.interscience.wiley.com).

ABSTRACT: A modified version of the two-phase flow-induced crystallization model of Doufas et al. (J Non-Newtonian Fluid Mech 2000, 92, 27) for melt spinning of polymeric fibers is presented to address three issues: (1) discontinuities generated due to the imposition of continuation conditions at the crystallization onset at T_m^o; (2) excessive strength of the flow enhancement component coupling the total extra stress tensor invariant to the crystallization kinetics; and (3) Avrami isotherms used. The modified model provides seamless, two-phase predictions for all-state variables in the fiber-spinning process and significantly reduces discontinuities. Moreover, a new component for the flow-induced crystallization rate and Avrami crystallization rate isotherms increase the predictive capability of the model. Quantitative prediction of the velocity, stress, temperature, density (or crystallinity), and birefringence profiles are demonstrated for Nylon 66 and PET melts for a variety of process conditions, including predictions of quenched-sample density profiles and the take-up speed dependence of as-spun fiber density. The new algorithm, assisted by the coupling model, provides a more efficient and robust convergence of steady-state calculations and has been tested to predict spinning phenomena up to spin speeds of 9000 m/min. © 2006 Wiley Periodicals, Inc. J Appl Polym Sci 100: 3240–3254, 2006

Key words: fiber; modeling; crystallization; processing; necking

INTRODUCTION

Melt spinning of semicrystalline fibers is one of the most commercially important industrial polymer processes. It is well-known that flow-induced crystallization (FIC) plays a controlling role in the development of fiber properties, particularly under high-speed spinning conditions. Hence, the ability to quantitatively model FIC in melt spinning offers the opportunity for optimization of the process as well as providing a fundamental framework for addressing other polymer processes involving FIC. As will be shown in this article, crystallization along the fiber spinline is initiated by thermal, Avramian effects, which are then enhanced by chain stretching, particularly under high-speed conditions, leading to an increase in the stored free energy. For this reason, we believe that FIC may be more accurately described as FEC or flow-enhanced crystallization.

The major challenge in modeling FIC or FEC has been determining the proper coupling of the crystallization (flow-enhanced and isotropic) with spinline velocity and stress fields in the absence of a fundamental theory that would be able to describe the crystallization rate and rheology of the semicrystalline system from first principles. In a recent series of papers,[1–3] Doufas et al. described a two-phase model for FIC based on separate constitutive equations for the untransformed melt and semicrystalline phases. Their approach represents a significant advance over prior models since, among other things: it has a microstructural base that allows coupling of fiber structure (molecular orientation and crystallinity) with the macroscopic velocity, stress, and temperature fields. Most especially, the model was shown to quantitatively fit and predict spinline data for rapid crystallizing (nylon) and slow crystallizing (PET) systems under a wide range of operating conditions, including low- and high-speed spinning conditions. Their simulations were the first to capture the necking phenomenon under high-speed conditions and relate it to the combined effects of viscoelasticity and crystallization. The model was shown to be applicable for both steady 1- and 2-D[4] analysis of the fiber-spinning process.

Despite these important advances, the Doufas et al.[1] algorithm for simulating steady-state fiber spinning produces some discontinuities, as will be illustrated in this work. In addition to the potential problem that would arise from the propagation of these discontinuities in a hyperbolic system of partial differential

**Present address:* GE Water & Process Technologies, Chemistry and Microbiological Detection Technology, 4636 Somerton Road, Trevose, PA 19053.

Correspondence to: A. J. McHugh (ajm8@lehigh.edu).

Contract grant sponsor: ERC program of the National Science Foundation; contract grant number: EEC-9731680.

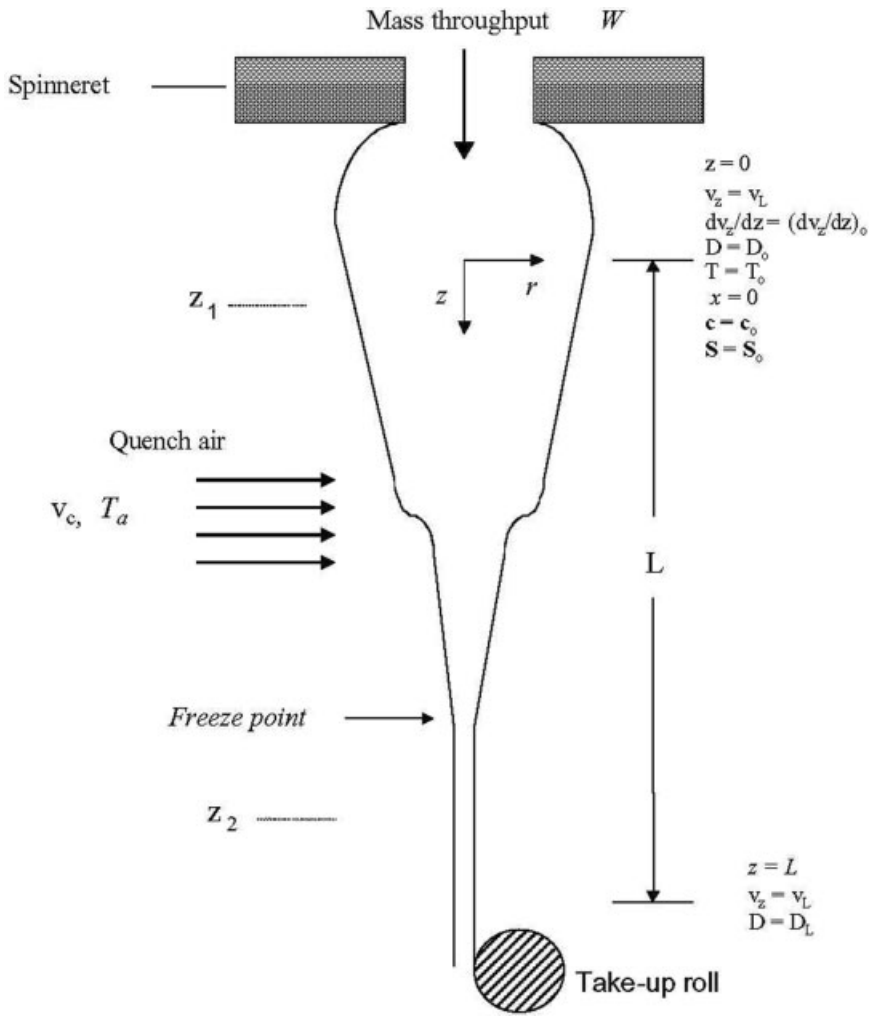

Figure 1 Schematic representation of a one-dimensional single filament melt-spinning model. See text for further detail.

equations (PDEs), the extremely small spatial steps required to overcome them imposes prohibitive storage requirements, thereby, limiting the ability to carry out complete dynamic analyses. These problems reflect basically two features of the algorithm. The first is associated with the specification of the crystallization onset, which is a location along the spinline where the fiber temperature drops to the equilibrium melting point. The second is related to the inclusion of the semicrystalline constitutive stress in the FEC component, which, as will be shown in this study, produces an overly strong coupling of the stress with the crystallization kinetics, ultimately leading to a nonzero transformation rate even as complete transformation is attained along the spinline. As a consequence the transformation rate needs to be annulled at that point, thereby limiting the ability of the model to predict take-up speed dependence in the final crystallinity under high-speed conditions.

The object of this study is to present a new algorithm that overcomes these problems. The key features to be illustrated are: (i) a framework for the introduction of crystallization from the beginning of the spinline, (ii) a new coupling component for FEC based on the melt-phase stored free energy for elastic dumbbells, which assists the seamless evolution of the two-phase model, and (iii) use of Avrami crystallization kinetics to predict the thermally driven crystallization.

MODEL BACKGROUND

The model development and equations for the 1-D thin-filament approximation shown in Figure 1 are addressed in detail in Doufas et al.[1] We adopt the same dimensionless state variables here (see Nomenclature); however, initial conditions are modified to allow the crystallization to start from the beginning of the spinline.

The seven steady-state variables are classified as: *macroscopic*, axial velocity v_z^* and strain rate dv_z^*/dz^*, temperature T^*; *microstructural*, melt (untransformed)

phase conformation tensor $\mathbf{c}^*$ (zz and rr components), semicrystalline phase orientation tensor $\mathbf{S}$ (zz component), and degree of transformation x. In this model, crystallization corresponds to the transfer of N statistical segments (out of a statistical N_o-segment chain initially present in the melt) from the melt phase to the semicrystalline phase. The degree of transformation x is defined as the fraction of statistical segments that have transformed at any time ($x \equiv N/N_o$). The degree of transformation (x) is also equivalent to the relative crystallinity ($x = \phi/\phi_\infty$, where ϕ is the absolute degree of crystallinity), assuming that the semicrystalline phase can be characterized by an internal degree of equilibrium crystallinity ϕ_∞, which is taken as a constant.[5,6]

In the earlier model,[1] an onset criterion for initiating crystallization was imposed at a point where the fiber temperature drops to the equilibrium melt temperature $T_m{}^o$. This onset criterion is essentially a "switch-like" boundary condition on temperature requiring different sets of transport and constitutive/microstructural equations to be solved on either side (preonset and postonset) of this point. Continuation of the axial velocity $v_z{}^*$ and strain rate $dv_z{}^*/dz^*$ was ensured across the onset boundary by means of initializing postonset transport equations with analogous quantities from the preonset equations; however, the algorithm did not ensure robust initialization of continuation conditions for certain other state variables and their relevant gradients required to integrate the postonset transport and constitutive/microstructural equations (this point is further discussed in a later section).

In the following sections, a single set of 1-D transport and constitutive/microstructural equations to be used across the entire spinline is presented. With this framework for initiating the crystallization and FEC components, a seamless model results, eliminating the need for the crystallization onset and termination criteria. The seamless model also replaces the three sets of equations (preonset, postonset, and postermination) with a single set of equations. This is followed by a new algorithm introduced to determine consistent initial conditions for incorporating the semicrystalline phase seamlessly at $z = 0$. The new framework allows the crystallization rate to naturally evolve and exhibit an onset of crystallization, taking advantage of the Avrami crystallization rate isotherms. Specifically related to the crystallization rate, (i) a flow-coupling model (FEC component) based on the stored free energy of elastic dumbbells in the melt phase is used for coupling enhancement due to flow with the Avrami crystallization-rate, and (ii) Avrami rate isotherms available from literature[7] are used instead of those available from DuPont.[8] Finally, extensive comparisons of the predictions of the present approach are discussed.

Governing transport and constitutive/microstructural equations

The general unsteady-state defining transport and microstructural equations for the 1-D model are given in this section. All quantities and dimensionless numbers (denoted by D_i) used here are defined in the Nomenclature section.

Mass balance

$$\frac{W^*}{v_z^*}\left(\frac{1}{W^*}\frac{\partial W^*}{\partial t^*} - \frac{1}{v_z^*}\frac{\partial v^*}{\partial t^*}\right) + \frac{\partial W^*}{\partial z^*} = 0 \tag{1}$$

Momentum equation

The axial momentum balance equation given below includes all secondary forces, namely, surface tension, air drag, and inertia.

$$D_1\left(\frac{\partial v_z^*}{\partial t^*} + v_z^*\frac{\partial v_z^*}{\partial z^*}\right) = \left[D_4\left(\frac{1}{v_z^* W^*}\right)^{1/2} + \left(\frac{\tau_{zz}^* - \tau_{rr}^*}{v_z^*}\right)\right] \times \left(\frac{v_z^*}{W^*}\frac{\partial W^*}{\partial z^*} - \frac{\partial v_z^*}{\partial_z{}^*}\right) + \frac{\partial(\tau_{zz}^* - \tau_{rr}^*)}{\partial z^*} - \frac{D_2 v_z^*(v_z^* - v_d^*)}{W^*} + D_3 \tag{2}$$

Energy balance

$$\frac{1}{v_z^*}\left(\frac{\partial T^*}{\partial t^*} + v_z^*\frac{\partial T^*}{\partial z^*}\right) = -D_5(W^* v_z^*)^{-1/2}(T^* - T_a^*) + D_6\frac{\tau_{zz}^* - \tau_{rr}^*}{v_z^*}\frac{\partial v_z^*}{\partial z^*} + D_7\frac{1}{v_z^*}\frac{Dx}{Dt^*} \tag{3}$$

In the above expression, the crystallization rate is given by the substantial derivative of the fraction transformed, $\frac{Dx}{Dt}$.

Extra stress tensor

The constitutive stress equation for the semicrystalline system contains parallel contributions from the two phases: the "untransformed," amorphous melt (a) phase assumed to consist of elastic dumbbells, and the semicrystalline (sc) phase, assumed to consist of rigid-rods. Thus, the total stress is given by the following equations.

$$\tau^* = \frac{1}{1-x}\mathbf{c}^* - \boldsymbol{\delta} + 3\mathbf{S} + 6Deb_{sc}\mathbf{B} \tag{4a}$$

where

$$Deb_{sc} = c\, Deb_o\,[a'(T^*)\exp(Fx)] \tag{4b}$$

and

$$\mathbf{B} \equiv (\nabla^*\mathbf{v}^*)^{\mathbf{T}}:\langle \mathbf{uuuu}\rangle$$

$$\equiv (\mathbf{1}-w)\left\{\frac{1}{15}\left((\nabla^*\mathbf{v}^*)+(\nabla^*\mathbf{v}^*)^{\mathbf{T}}\right) + \frac{\mathbf{1}}{7}\begin{bmatrix} ((\nabla^*\mathbf{v}^*)^T:\mathbf{S})\boldsymbol{\delta} \\ +\mathbf{S}\cdot((\nabla^*\mathbf{v}^*)+(\nabla^*\mathbf{v}^*)^T) \\ +((\nabla^*\mathbf{v}^*)+(\nabla^*\mathbf{v}^*)^T)\cdot\mathbf{S} \end{bmatrix}\right\} + \mathbf{w}((\nabla^*\mathbf{v}^*)^T:\mathbf{S})\left(\mathbf{S}+\frac{\mathbf{1}}{\mathbf{3}}\boldsymbol{\delta}\right) \tag{4c}$$

$$w = 1 - 27det\left(\mathbf{S}+\frac{\mathbf{1}}{\mathbf{3}}\boldsymbol{\delta}\right) \tag{4d}$$

The term, $a'(T^*)$, in eq. (4b) is a shift factor for the temperature dependence of viscosity and Deb_o is the Deborah number ($= v_o\lambda_a/L$, where λ_a is the relaxation time of the melt). In eq. (4a), the melt stress equation used is a "modified" version of the Giesekus stress constitutive equation for elastic dumbbells, to account for the effect of phase transformation on the Hookean spring constant K[1]. Doufas et al.[1] had further modified the Giesekus equation to incorporate the nonlinear spring constant or Peterlin factor E in the expressions for the melt stress and conformation tensors. The latter was needed under high-spin speed conditions where, as noted earlier, the model predicted 100% transformation ($x \sim 1$). Under these conditions, the melt-phase chains approached zero length; hence, the Peterlin factor was needed to correct for the nonlinearity in the force-extension behavior. However, as will be shown in this work, with the modified model, x remains less than one, leading to a locking-in of the system with negligible nonlinear effects in the melt phase.

The closure approximation used in eqs. (4c and 4d) is the same as that used earlier.[1] Acknowledging that the orientation tensor **S** is traceless and further utilizing simplifications for extensional flow geometry, i.e., equal rr and $\theta\theta$ components, the rheological force and coupling invariants can be expanded as eq. 5 below:

$$\tau^*_{zz} - \tau^*_{rr} = \frac{c^*_{zz} - c^*_{rr}}{1-x} + 4.5S_{zz} + 6Deb_{sc}(B_{zz} - B_{rr}) \tag{5a}$$

$$tr\,\tau^* = \frac{tr\,c^*}{1-x} - 3 + 6Deb_{sc}\,tr\,\mathbf{B} \tag{5b}$$

$$B_{zz} = \left\{(1-w)\left[\frac{2}{15}+\frac{11}{14}S_{zz}\right] + w\frac{3}{2}S_{zz}(S_{zz}+1/3)\right\}\frac{\partial v^*_z}{\partial z^*} \tag{5c}$$

$$B_{rr} = \left\{(1-w)\left[-\frac{1}{15}+\frac{5}{14}S_{zz}\right] + w\frac{3}{2}S_{zz}(-S_{zz}/2+1/3)\right\}\frac{\partial v^*_z}{\partial z^*} \tag{5d}$$

$$tr\,\mathbf{B} = \left\{\frac{\mathbf{3}}{\mathbf{2}}S_{zz}\right\}\frac{\partial v^*_z}{\partial z^*} \tag{5e}$$

Equation (5a) represents the primary rheological force driving the fiber-spinning process and eqs. (5c and 5d) are expressions of the semicrystalline stress closure approximation term also used later in the orientation S evolution equation (see eq. 7). Equations (5b and 5e) constitute the first invariant of the total constitutive extra stress of the two phases, which was used in the earlier model[1] as the coupling term for FEC. The dimensionless coefficients and Deborah numbers in the above equations are defined in the Nomenclature.

Microstructural evolution equations for c^*_{zz} and c^*_{rr}

$$\frac{1}{v^*_z}\left(\frac{\partial c^*_{zz}}{\partial t^*} + v^*_z\frac{\partial c^*_{zz}}{\partial z^*}\right) = 2\frac{c^*_{zz}}{v^*_z}\frac{\partial v^*_z}{\partial z^*} - \frac{1-x}{v^*_z Deb_a}\left((1-\alpha)+\alpha\frac{c^*_{zz}}{1-x}\right)\left(\frac{c^*_{zz}}{1-x}-1\right) \tag{6a}$$

$$\frac{1}{v^*_z}\left(\frac{\partial c^*_{rr}}{\partial t^*} + v^*_z\frac{\partial c^*_{rr}}{\partial z^*}\right) = -\frac{c^*_{rr}}{v^*_z}\frac{\partial v^*_z}{\partial z^*} - \frac{1-x}{v^*_z Deb_a}\left((1-\alpha)+\alpha\frac{c^*_{rr}}{1-x}\right)\left(\frac{c^*_{rr}}{1-x}-1\right) \tag{6b}$$

Evolution equation for s_{zz}

$$\frac{1}{v^*_z}\left(\frac{\partial S_{zz}}{\partial t^*} + v^*_z\frac{\partial S_{zz}}{\partial z^*}\right) = -\frac{1}{v^*_z Deb_{sc}}S_{zz} + \frac{(2/3+2S_{zz})}{v^*_z}\frac{\partial v^*_z}{\partial z^*} - 2\frac{B_{zz}}{v^*_z} \tag{7}$$

The parameter σ used in the earlier model[1–3] to fit birefringence profiles has been set to unity in the present model. Also, the amorphous-phase Deborah number, Deb_a, eqs. (6a and 6b), is written in terms of the amorphous-phase relaxation time scaled with respected to its quadratic dependence on the degree of transformation[1] (See also Nomenclature).

Birefringence calculation

Birefringence is calculated using the earlier method[1–3]; however, in the absence of the Peterlin nonlinearity factor E, the melt contribution is altered[7] to give the following expression:

$$\Delta n = \Delta_m^0(0.6/N_o)(c_{zz}^* - c_{rr}^*)/tr\ \boldsymbol{c}^* + \Delta_{sc}^0 x(1.5S_{zz}) \quad (8)$$

Density (crystallinity) calculation

To compare against reported measurements of quenched samples at various spinline positions, the following expression for the density of the semicrystalline fiber can be used.

$$\rho = (1 - \phi)\rho_a + \phi\rho_c \quad (9)$$

In this expression, ρ_a and ρ_c are the amorphous and pure crystal densities, respectively.

MODIFICATIONS

A free-energy based FEC component

A key issue in FIC or FEC is determining the proper coupling of the crystallization (flow-enhanced and isotropic) with velocity and stress fields in the absence of a fundamental, first principles theory. In the earlier version of the FEC model,[1] coupling was achieved through use of a term in the exponential of the total stress tensor in the overall Avrami rate expression. However, as mentioned in the Introduction, we now realize that this produces an overly strong coupling of the stress to the crystallization rate, leading to a nonzero transformation rate even as complete transformation is achieved along the spinline. Earlier considerations by one of us,[9] based on a combination of nucleation theory and stored free energy arguments, suggests that the exponential enhancement factor should be expressed solely in terms of the stored free energy of the stretched chains in the molten phase. Thus the appropriate expression for 1-D growth under flow becomes the following,

$$\frac{Dx}{Dt} = K^*(1 - x)\exp(2\xi a^*) \quad (10)$$

where a^* is the stored free energy of the melt phase, and ξ is the flow coupling parameter. In this form K^* ($= K_{av}\ L/v_o$) is the temperature-dependent Avrami factor for quiescent crystallization. The temperature dependence in K_{av} is assumed to be a Gaussian function.[7]

$$K_{av}(T) = K_{max}\exp[-4\ \ln(2)(T - T_{max})^2/D^2] \quad (11)$$

The factor of 2 in eq. (10) arises from the relationship between the stored free energy and melt-phase stress.[10]

$$a = \frac{1}{2}\mathrm{tr}\tau_a \quad (12)$$

With regard to the stress term in eq. (12), earlier arguments based on the Hamiltonian/Poisson bracket formalism[11] dictate that it is to be associated with the Helmholtz free energy of the melt phase, and should therefore contain only conservative terms. Since the mobility anisotropy introduced through the parameter α, which was incorporated in the elastic dumbbell stress constitutive equation to obtain eq. (5a) and eqs. (6a and 6b), represents a dissipative contribution,[11] the stress needed in eq. (12) should be that associated with the Maxwell or elastic dumbbell stress for the continuum. Derivation of the evolution equation for the stored free energy starts with the following forms for the conformation tensor evolution equation and the associated stress tensor.

$$\boldsymbol{c}_{(1)} = -\frac{1}{\lambda_a}\left[\boldsymbol{c} - \frac{k_BT}{K}\delta\right] \quad (13)$$

$$\tau = \frac{G\ K}{k_BT}\left(\boldsymbol{c} - \frac{k_BT}{K}\delta\right) \quad (14)$$

In these expressions, K and λ_a are the Hookean spring constant and relaxation time for the melt phase, respectively, and G is the shear modulus. Following the steps outlined in the work of Marucci[10] leads to the following expression for the free energy evolution under flow.

$$\frac{Da^*}{Dt^*} = \frac{c^*:\nabla^* v^*}{1 - x} - \frac{a^*}{\mathrm{Deb}_a(T,x)} \quad (15)$$

In eq. (15), the expressions for the spring constant, K, and melt-phase relaxation time that correct for the degree of transformation as defined in the earlier model[1] have been used.

With the two modifications discussed thus far in this Section, the crystallization process can evolve naturally at all points along the spinline with a single set of equations, thereby, eliminating two "switch-like" conditions, i.e., the onset and termination criteria.

An algorithm for the initial conditions

The fiber-spinning problem as defined constitutes a set of six steady-state ordinary differential equations (ODEs), including four evolution equations for the independent microstructural variables of the two phases and two transport equations, viz., axial momentum and energy. For numerical convenience, the first transport equation, which is a second-order ODE in velocity, is split into two first-order ODEs, thereby resulting in a system of seven first-order ODEs. Because of the hyperbolic nature of the full set of dynamic equations, it is desirable to obtain seamless steady-state predictions of all process and microstruc-

ture variables, thereby eliminating any "kinks" or discontinuities that arise due to uncertainty in the initial conditions, i.e., x_o, $c_{zz,o}$, $c_{rr,o}$, and $S_{zz,o}$. The determination of these quantities consistent with the momentum equation is a key to avoiding most of the initiation instabilities. Additional conditions need to be devised and solved simultaneously in an iterative scheme to obtain the "unknown" initial microstructure variables and the initial slope of velocity needed to consistently solve the system of steady-state equations.

Since the conformation tensor components are approximately unity at the spinneret exit, the trace of the melt stress tensor and the initial free energy will be approximately zero. Thus, the FEC component in eq. (10) is essentially unity at $z = 0$. We initialize the degree of transformation $x_o = 0$ since no nucleates are expected to have formed at the extrusion temperature at the spinneret die exit. Since the FEC component is unity at $z = 0$ ($a^* \to 0$), the gradient $(dx/dz^*)_o$ starts out primarily as Avramian, which is typically very small ($\sim 10^{-3}$ for Nylon 66 and $\sim 10^{-5}$ for PET).

To address the initialization of the other microstructural equations, we illustrate as an example, the evolution of the gradient of the orientation tensor **S**. In this case, the choice of $S_{zz,o} = 0$ (and consequently $w_o = 1$) yields a high positive $(dS_{zz}/dz^*)_o$ due to the second term on the right-hand side of eq. (7). This presents itself in the algorithm of the earlier model[1] at the point of crystallization onset where continuation equations that include the presence of the semicrystalline phase need to be explicitly initialized. Since our modification allows the presence of the semicrystalline phase at $z = 0$, a typical high-speed simulation using $S_{zz,o} = 0$ would exhibit a similar large $(dS_{zz}/dz^*)_o$ followed by a sharp decline to a value near zero within 10^{-4} of the total spinline distance, and finally a natural Gaussian evolution that leads to orientation lock-in.

To address the discontinuity in S_{zz} and other variables, three additional conditions need to be devised for the unknown initial conditions, viz., $S_{zz,o}$, $c_{rr,o}$, and $(dv_z^*/dz^*)_o$. This can be done by partitioning the axial momentum balance [eq. (2)] at $z^* = 0$ into three equations for an equal number of unknowns. The first partitioning omits terms from eq. (2) associated with the presence of the semicrystalline phase and air-drag, and represents, in effect, a balance on the amorphous phase. Thus, after expansion of the stress derivative and factoring, one has,

$$D_1 v_{z,0}^* \left(\frac{dv_z^*}{dz^*}\right)_o = \left[D_4 \left(\frac{1}{v_{z\rho}^*}\right)^{1/2} + \left(\frac{c_{zz,o}^* - c_{rr,o}^*}{v_{z,o}^*}\right)\right] \left(\frac{\partial v_z^*}{\partial z^*}\right)_o + \left[\frac{\partial (c_{zz}^* - c_{rr}^*)}{\partial z^*}\right]_o + D_3 \quad (16)$$

This expression is consistent with the assumption that, for uniaxial flow, $(dc^*_{rr}/dz^*)_o$ is expected to be a small negative number. The next partitioning isolates the second derivative in terms of factors associated with the nonisothermal rheology (i.e., velocity gradient and temperature dependence of the viscosity) and is written as

$$\left(\frac{d^2 v_z^*}{dz^{*2}}\right)_o = \frac{1}{v_z^*}\left(\frac{dv_z^*}{dz^*}\right)_0^2 + \frac{E^*}{(T_o^*)^2}\left(\frac{dT}{dz^*}\right)_o \left(\frac{dv_z^*}{dz^*}\right)_o \quad (17)$$

The remaining terms form the final partitioning as,

$$-F\, Deb_{sc,o} F_\Delta(S_{zz,o}) \left(\frac{dx}{dz^*}\right)_o \left(\frac{dv_z^*}{dz^*}\right)_o - Deb_{sc,o} \left(\frac{dF_\Delta(S_{zz})}{dS_{zz}}\right)_o \left(\frac{dS_{zz}}{dz^*}\right)_o \left(\frac{dv_z^*}{dz^*}\right)_o + 4.5 \frac{S_{zz,o}}{v_{z,o}^*}\left(\frac{dv_z^*}{dz^*}\right)_o - 4.5\left(\frac{dS_{zz}}{dz^*}\right)_o = 0 \quad (18)$$

where $F_\Delta = 6\dfrac{(B_{zz,o} - B_{rr,o})}{(dv_z^*/dz^*)_o}$. Equation (18) includes all terms that under any arbitrary transformation represent solely the semicrystalline phase, i.e., are associated with x or S_{zz}. Equation (18) is consistent with both the orientation (S_{zz} component) and its slope being slightly positive. Equations (16–18) constitute the coupled conditions to be solved simultaneously to obtain the three unknowns mentioned earlier, i.e., $c^*_{rr,o}$, $S_{zz,o}$, and $(dv_z^*/dz^*)_o$. While solution requires an estimate for the second derivative in the left side of eq. (17), experience has shown that convergence to final results is essentially insensitive to the values selected. Within this framework, the algorithm brings consistency between "unknown" initial conditions (these are required as continuation conditions in the earlier model[1]) and the single set of steady-state equations used for the fiber-spinning process.

CALCULATIONS AND PREDICTIONS

Input parameters

There are three types of inputs to the melt-spinning simulations: (1) physical/rheological parameters of the materials, (2) processing parameters, and (3) model parameters.

Physical/rheological parameters: modified Avrami crystallization kinetics

All physical and rheological parameters for Nylon 66 and PET given in the work of Doufas et al.[2,3] are used with the exception of properties listed in Table I. The values used for the intrinsic birefringence for the semicrystalline phase Δ_{sc}^o were estimated for Nylon 66 grades and PET by fitting profiles to the plateaus of

TABLE I
Material Properties for Nylon 66 and PET (All Other Properties Are Given Elsewhere[2,3])

Parameter	Nylon 66	PET
K_{max} (s^{-1})	1.64[7]	0.016[7]
D (°C)	80[7]	64[7]
T_{max} (°C)	150[7]	190[7]
ϕ_∞	0.5[8]	0.42[3]
Δ^o_{sc}	0.061 (0.057)[a]	0.188
ρ_a (g/cc)	1.09[13]	1.340[12]
ρ_c (g/cc)	1.24[13]	1.455[12]

[a]Nylon 66-A.

birefringence data given in Figures 3 and 6 below, respectively, and are reasonably within bounds of the inequality, $\phi_\infty\Delta^o_c < \Delta^o_{sc} < \Delta^o_c$. The temperature dependencies of the viscosities for Nylon 66 and PET are given by the shift factor functions:

$$a' = \exp\left[\frac{E_A}{RT_o}\left(\frac{1}{T^*} - \frac{1}{T^*_r}\right)\right] \tag{19a}$$

and

$$a' = \exp\left[\frac{E_A}{RT_o}\left(\frac{1}{T^* - T^*_r} - \frac{1}{T^*_m - T^*_r}\right)\right] \tag{19b}$$

respectively.

Processing parameters

All processing parameters for the results presented in the next section were the same as those used earlier.[2,3]

Model: fixed and fitting parameters

The model parameters used for the Nylon 66 and PET runs are labeled as *fixed*—-meaning once determined for a given run, they were held constant for all remaining runs, and *tuning*—-meaning they were varied according to the run conditions to obtain optimal fits. These are summarized in Tables II (fixed) and III (tuning).

The only parameter used for tuning the Nylon 66 and Nylon 66-A grades having different RV (reduce viscosity) values is the coupling parameter, ξ. The Giesekus parameter,α, which introduces a quadratic stress term in the elastic dumbbell constitutive equation based on anisotropic chain mobility, is set at 0.5 and 0.3 for Nylon 66 and PET, respectively. As indicated in Table II, the coupling stress parameter, ξ, is fixed for PET since the variation in intrinsic viscosity values was not significant; however, in the case of Nylon 66, ξ is allowed to vary with RV. The ξ parameter in general increases with increasing RV value (the value at lowest RV being an exception) suggesting that it might be possible to reduce or eliminate this parameter by incorporating effects such as an M_w dependence in the shear modulus, G_o, corresponding to the different RV values.

TABLE II
Fixed Model Parameters

Parameter	Nylon 66	Nylon 66-A	PET
α	0.5	0.5	0.3
F	20	20	50
σ	1.0	1.0	1.0
c	0.02	0.10	0.03
ξ	See Table 3	See Table 3	0.097

TABLE III
Variation of "Tuning" Coupling Parameter ξ with RV

RV	Tests	Nylon 66	Nylon 66-A
37.5	S06, S08[a]	0.112	0.134
45.0	S10[a]	–	0.136
52.5	S01–S03	0.072	–
68.0	S04–S05	0.080	–
70.0, 72.0	S12–S20	0.083	–

[a]Nylon 66-A.

Combined low and high-speed predictions (Nylon 66 grades and PET)

The modified model was benchmarked with the complete set of test runs for Nylon 66 (virgin homopolymer and homopolymer *w/additives*) and PET used in the previous studies.[2,3] In this section, we present an overview of our results to demonstrate the capability of the modified model.

As demonstrated through the excellent quantitative predictions in Figures 2–6, it is possible to predict fiber-spinning phenomena from low-to-high speeds, and at various mass throughputs, using a single set of parameters. We also note from Figure 2 that the velocity locks in with a relatively more mild curvature just before it approaches the take-up velocity, in agreement with the experimental data. The modification of the coupling model also enables simultaneous quantitative predictions of the density (or crystallinity) profile data of Vassilatos et al.,[12] which is demonstrated in Figure 3. The model also predicts the effect of cooling air velocity (or air drag) and the effect of spinneret diameter (Figures not shown) with the same set of parameters summarized in Tables II and III. This is an improvement over the earlier version where up to three tuning parameters were required to capture the effect of throughput variation. In addition, we have less overall model parameters (a total of four): α, F, c, and ξ of which the first three are fixed, based on the material, and only one parameter ξ is tuned to incorporate variations in RV (or molecular weight).

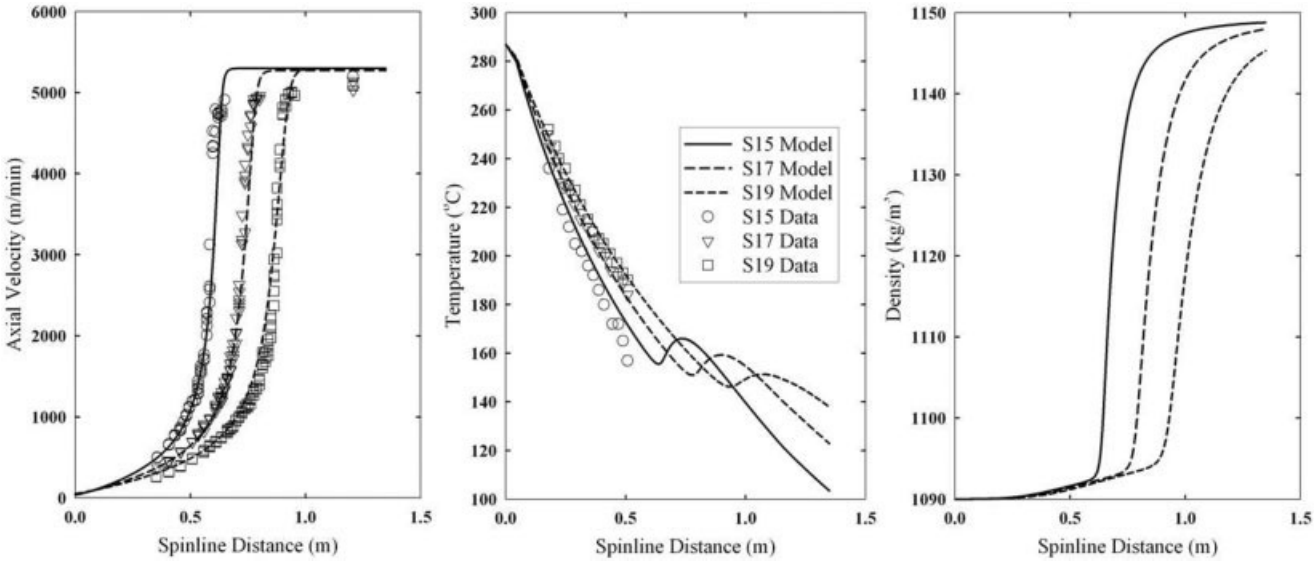

Figure 2 Prediction of Nylon 66 high-speed spinning profiles with a single parameter set, including the prediction of the effect of throughput on velocity, temperature, and density profiles. Run conditions correspond to those given in Ref. [2]

The general features for low-speed fiber spinning are very similar to those shown earlier.[2,3] It is seen that FEC is not a significant factor at these low speeds, i.e., the Avramian rate is dominant. Therefore, a concentrated neck is not observed (See Figs. 4 and 5). This point is further illustrated by examining the predictions for the evolution of the crystallization gradient for low- to very high-speed spinning (shown later in Figs. 10 and 11). An important point to emphasize is that we do not tune any parameters to obtain predictions for the low-speed test runs, rather a single set of parameters (see Tables II and III) is able to accurately describe most experimental velocity/diameter, birefringence, temperature, and density profiles for both low- and high-spin speeds.

Calculated temperature profiles are also in good agreement with experimental data. Unfortunately, temperature measurements from these tests are not available in the vicinity of the characteristic peak or "bump" where the FEC peak also occurs; however, our predictions clearly exhibit a natural crystallization peak of the order suggested by Haberkorn.[14] Moreover, the shift in the position of the peak shows the same trend with changing mass flow rate as the ve-

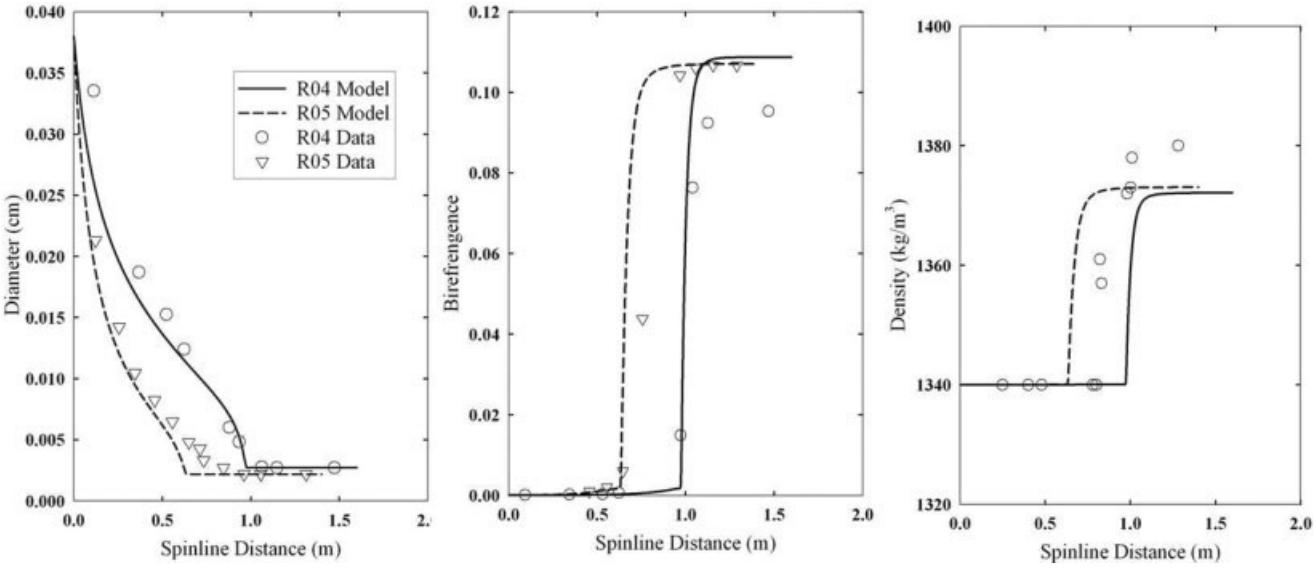

Figure 3 Prediction of PET high-speed spinning profiles (PET: IV = 0.650) with a single parameter set, including velocity, birefringence, and density profiles. Run conditions correspond to those given in Ref [12].

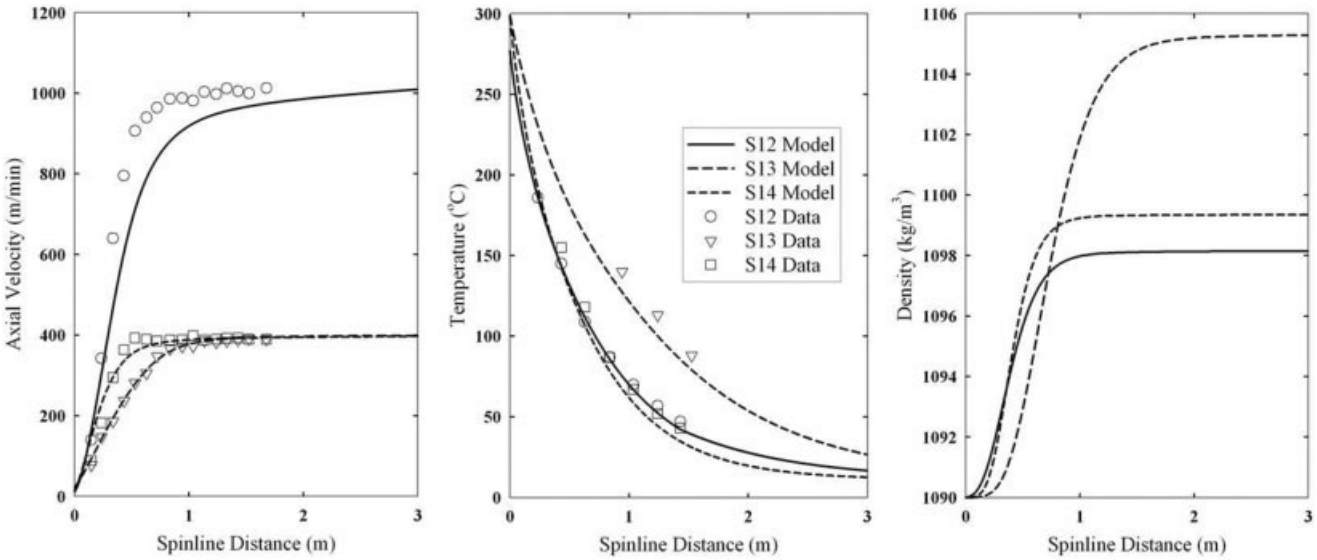

Figure 4 Prediction of Nylon 66 low-speed spinning profiles with the same set of parameters used in Figure 2 (for RV = 70.0), including velocity, temperature, and density profiles. Run conditions correspond to those given in Ref. [2].

locity neck (see Fig. 2), further confirming that FEC and the necking behavior are mutually interdependent.

The birefringence predictions for PET and Nylon 66 grades shown in Figures 3 and 6 are in excellent agreement with experimental data. The lower birefringence values predicted before the transformation sharply takes off and the prediction of a smooth curvature before freeze-off are captured very well. Thus, the modified model shows excellent predictive capability for a wide range of fiber-spinning phenomena, with a single and smaller set of parameters for Nylon 66, and only one "tuning" parameter ξ to incorporate variations in molecular weight. The intrinsic birefrin-

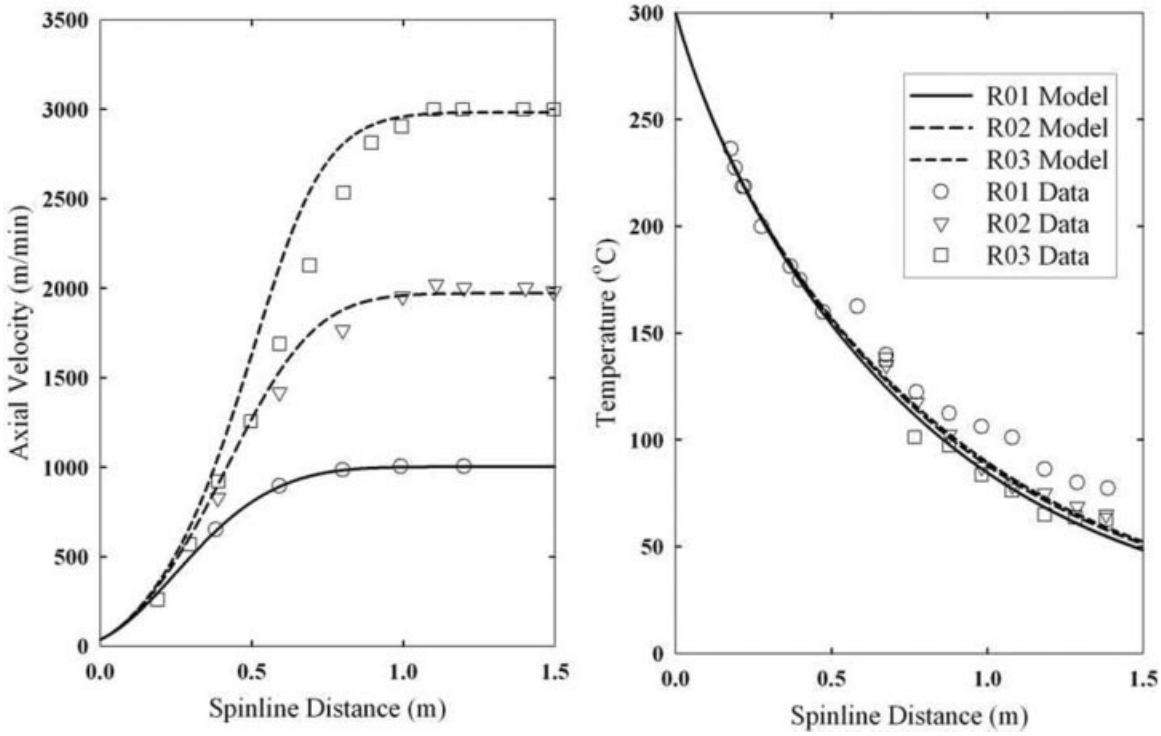

Figure 5 Prediction of PET low-speed spinning profiles (PET: IV = 0.675) with the same set of parameters used in Figure 3, including velocity and temperature profiles. Run conditions correspond to those given in Ref. [12].

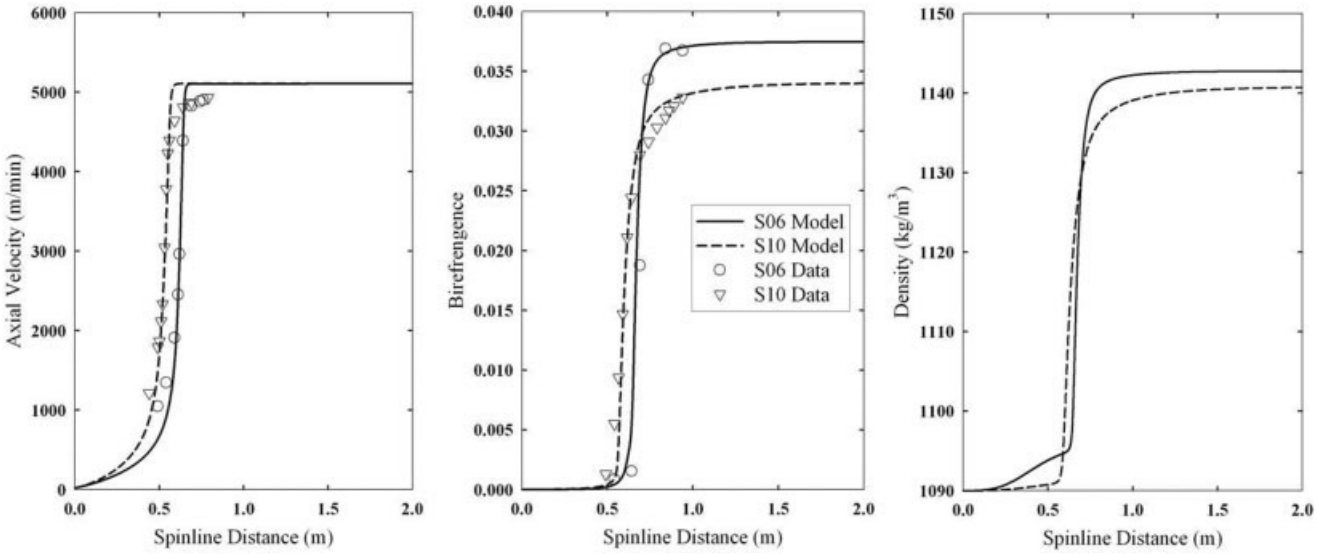

Figure 6 Prediction of high-speed spinning profiles for Nylon grades (Nylon 66 and Nylon 66-A), each with a single parameter set (see Tables II and III), including simultaneous velocity, birefringence, and density profiles. Run conditions correspond to those given in Ref. [2].

gence of the semicrystalline phase is estimated by fitting a single profile for each material. No parameter adjustments are required to describe the effect of variations in process conditions, thereby, providing a suitable framework for simulating spinline performance and optimization.

Material variations, such as the addition of nucleating agents (in the material denoted by Nylon 66-A), can be described solely by adjusting the parameter c, to incorporate the more viscous behavior, thereby resulting in drawing the neck closer to the spinneret die exit (see Fig. 6). With only one modified parameter, i.e., c, we are simultaneously able to predict profiles of velocity and birefringence for this grade of Nylon (Nylon 66-A: Nylon 66 w/additive). Moreover, the same parameters can quantatively predict other test runs (see Table II and III) for this same Nylon grade by tuning only parameter ξ and keeping all other model parameters unchanged.

Improved steady-state predictions

Elimination of discontinuities from steady-state calculations

Examples of the discontinuities produced in the earlier model are illustrated in Figures 7 and 8 comparing predictions for the conditions of run S01. While the velocity profiles for the two are nearly identical, the earlier model[1–3] exhibits a downward "spike" in the gradient of c^*_{rr} as the degree of transformation approaches unity, while the modified version exhibits a more continuous evolution. The profile in the original model reflects the response of the system to the competing effects of the uniaxial extension flow (positive strain rate in z-direction and negative in r-direction) and the loss of segments from the melt phase due to crystallization. The initial decrease in c_{rr}* (i.e., negative gradient) reflects the kinematics. However, in the region where x begins to approach unity, since c_{zz}* begins to significantly decrease, c_{rr}* must increase to satisfy incompressibility. In our modified model, the latter behavior does not occur since, x does not approach unity. Moreover, in consequence of this, the present model does not require an abrupt "switch-like" termination condition. The current algorithm also eliminates onset discontinuities, such as the one shown for slope of S_{zz} in Figure 7 that occurs due to the initialization of S_{zz} at the onset point where the semicrystalline phase is introduced.

As shown in Figures 2–3 and 6–8, the modified model is able to accurately capture the "concentrated" necking phenomena associated with high-speed spinning and freeze-off of the velocity (or diameter) profiles, which was also predicted by the earlier model. Figure 8 also illustrates the improved seamless prediction of the transformation rate compared to the presence of two "switch-over" points in the earlier predictions: the first associated with crystallization onset and the second with crystallization termination. The evolution of the transformation rate is related to the initiation of "concentrated necking" and freeze-off phenomena. The beginning of the neck occurs approximately where the transformation rate profile begins to deviate from the underlying Avramian transformation rate, which is indicated reasonably well (see also Figs. 10 and 11) by the dx/dz* evolution. On the other hand, freeze-off coincides well with the maximum in the FEC transformation rate. Moreover, all calcula-

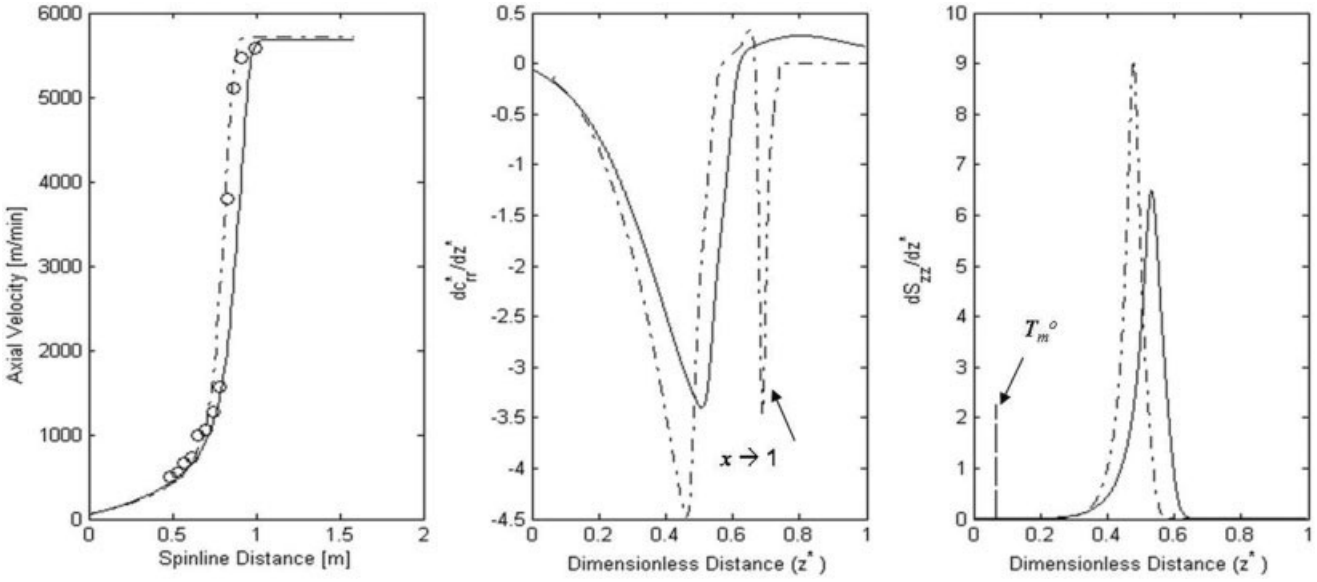

Figure 7 Comparison of predictions of c^*_{rr} and S_{zz} evolution equations for a typical high-speed run (labeled S01, (velocity data denoted by circle) for Nylon 66 using the present model (solid lines) and the model of Doufas et al. (dash-dotted lines).

tions are characterized by the seamless presence of the two-phases and a continuous transformation rate that has the ability to predict the transformation at all positions along the spinline. The Gaussian temperature dependence of the Avramian kinetics initially governs the crystallization rate until a point where the stress acting along the spinline is sufficient to cause enough chain extension and associated increase of the stored free energy to give rise to an FEC crystallization peak.

In the stress profiles shown in Figure 9, the contribution of the semicrystalline phase to the total $\tau_{zz}^* - \tau_{rr}^*$ is initially negligible, in agreement with the earlier model. The total extra stress difference $\tau_{zz}^* - \tau_{rr}^*$ profile predicted for the two models is nearly identical, which is consistent with the prediction of nearly identical velocity profiles; however, in the present model, the melt contribution freezes-off at a value one-to-two orders of magnitude lower than the total stress after exhibiting a maximum, rather than going to zero, which the earlier model predicts. Since the present model does not predict a complete transformation of the melt, it provides an opportunity to develop correlations of the two stress contributions at the take-up to end-properties of the fiber. A recent application of the modified algorithm to PLA fiber spinning utilizing a different melt-phase constitutive model has shown that this approach enables excellent correlation of elongation to break data.[15]

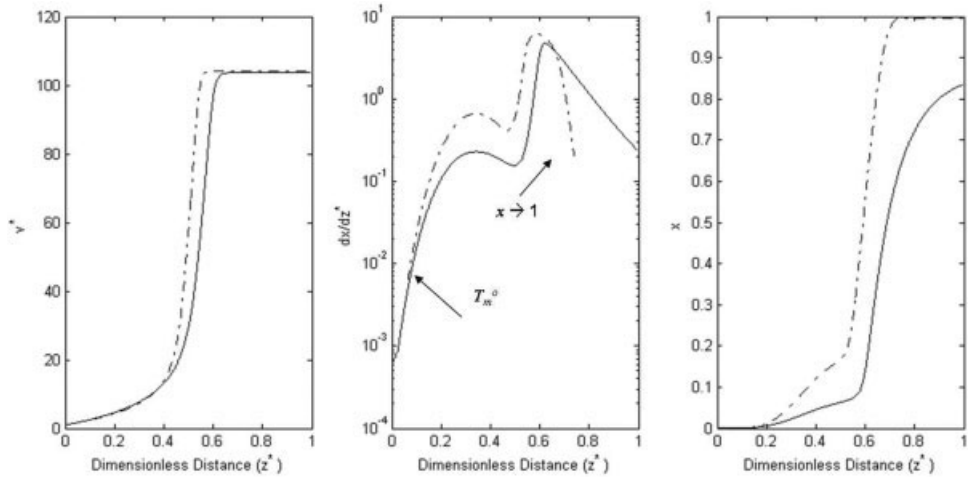

Figure 8 Comparison of velocity profiles, dx/dz^*, and x predictions of a typical high-speed run (labeled S01) for Nylon 66 using the present model (solid lines) and the earlier model[2] (dash-dotted lines).

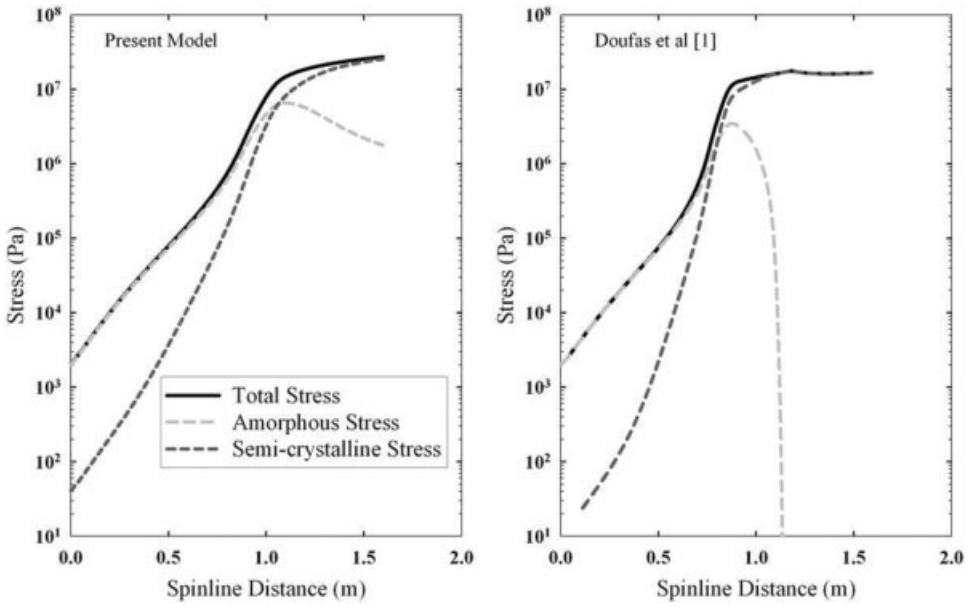

Figure 9 Comparison of the total extra stress difference (solid lines) and contributions of the melt phase (gray dotted lines) and the semicrystalline phase (black dotted lines) for a typical high-speed run (labeled S01) for Nylon 66 using the present model (left) and the model of Doufas et al. (right).

Effect of take-up velocity on the as-spun fiber crystallinity

Predictions of velocity and transformation rate profiles are shown in Figures 10 and 11 for Nylon 66 and PET, respectively. The transformation rate profiles suggest that the appearance of a strong FEC peak is also indicative of the occurrence of a concentrated neck. The maximum of the FEC peak coincides approximately with the freeze-off in the velocity profiles. These predictions are based on all conditions pertaining to test S01 for Nylon 66 and R05 for PET, respectively, only varying the take-up velocity. At low-speed spinning conditions, the Avramian evolution of the transformation rate is recovered and is the controlling feature of the crystallization. Also shown is the as-spun density for all take-up velocities between the

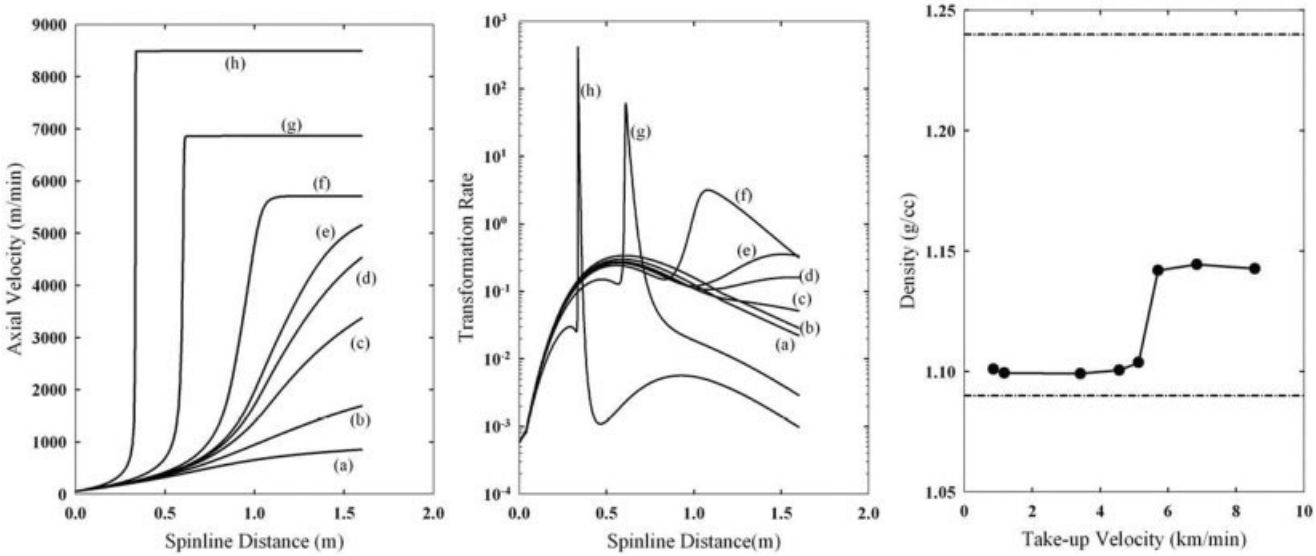

Figure 10 Model predictions of velocity and transformation rate profiles, and as-spun crystalline density for various take-up speeds based on all other conditions of test labeled S01 (Nylon 66). (a) = 855 m/min; (b) = 1710 m/min; (c) = 3420 m/min; (d) = 4560 m/min; (e) = 5130 m/min; (f) = 5700 m/min; (g) = 6840 m/min; (h) = 8550 m/min. Upper and lower dotted lines on density plot represent pure amorphous and crystalline phase densities, respectively.

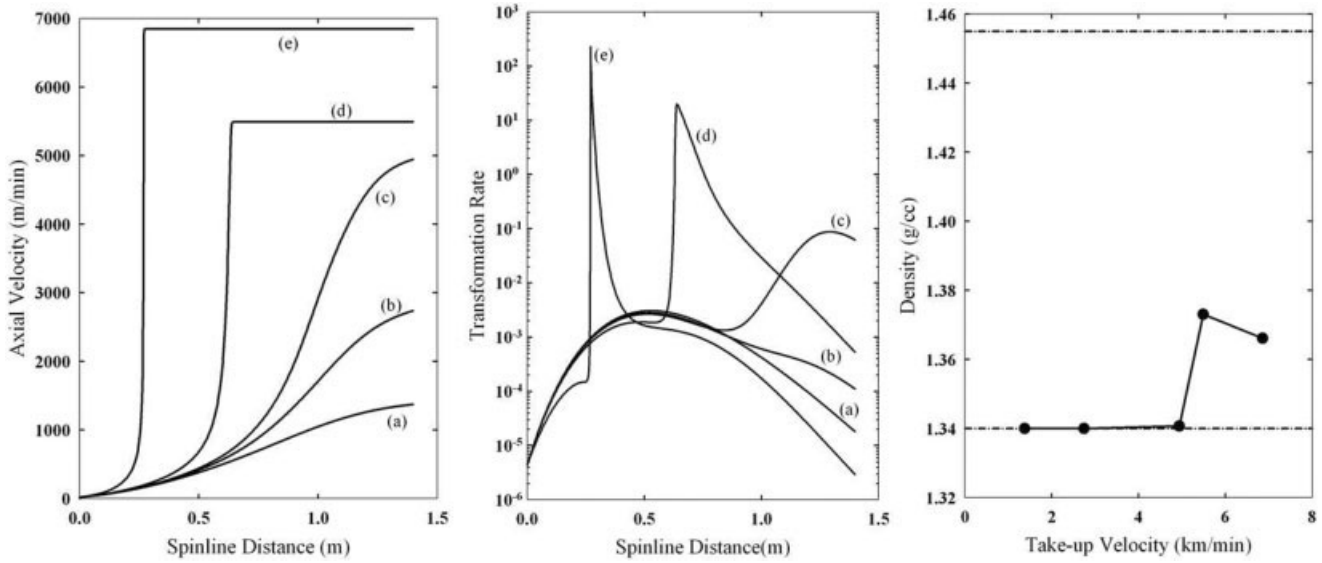

Figure 11 Model predictions of velocity and transformation rate profiles, and as-spun crystalline density for various take-up speeds based on all other conditions of test labeled R05 (PET). (a) = 1373 m/min; (b) = 2745 m/min; (c) = 4941 m/min; (d) = 5490 m/min; (e) = 6863 m/min. Upper and lower dotted lines on density plot represent pure amorphous and crystalline phase densities, respectively.

limits of perfect crystal density and amorphous density.

The transformation rate profiles provide an understanding of the underlying phenomena and structure development along the spinline. In agreement with experimental data,[16] the predictions suggest that for certain material characteristics and processing conditions, the as-spun crystallinity exhibits a maximum with take-up speed. The low-speed as-spun crystallinity for Nylon 66 is higher as compared with that for PET, because the Avramian effect dominates at low-speeds. Consequently, PET, being a slow-crystallizer under quiescent conditions, does not develop crystallinity to any significant extent at low speeds; however, FEC effects dominate at the higher spinning speeds and may produce an almost equal degree of transformation for both Nylon 66 and PET, regardless of the underlying Avrami crystallization rate.

A sharp rise in the as-spun density is predicted between 5000 and 6000 m/min for both Nylon 66 and PET. This basically demarcates the appearance of strong FEC effects. The specific velocity range for this transition can vary significantly with variations in processing conditions and material characteristics. Similar behavior patterns have been reported for the high-speed spinning of PET[16] and polyethylene naphthalate (PEN) fibers.[17]

Effect of avrami kinetic parameters

Sensitivity of the predictions of the modified model with K_{max} can be useful, since there may be some variations in the Avrami kinetic parameters from one experimental study to another. This sensitivity is best illustrated by considering a low-speed spinning profile where Avramian effects dominate. Figure 12 illustrates the effect of doubling and halving K_{max} from its value used in Table I and its effect on the velocity predictions for the Nylon 66 test run labeled S12. A higher K_{max} is able to more accurately reproduce the velocity profile for the low-speed run, thereby suggesting that accurate determination of K_{max} and its appropriate transformation from higher order quiescent crystallization kinetics to first-order growth in the fiber-spinning predictions shown in this study is of utmost importance.

CONCLUSIONS

In this study, we have presented a modified version of the two-phase model for flow-enhanced crystallization which is applied to fiber spinning of Nylon 66 grades and PET. The modified model accurately captures the general features of high-speed spinning. Significantly, a new algorithm and FEC coupling improves the predictive power of the two-phase formalism over the earlier model of Doufas et al.[1] The new algorithm also effectively eliminates discontinuities characteristic of the predictions of the earlier model for both the onset and completion of crystallization along the spinline. The new FEC component based on the melt-phase stored free energy, applied in conjunction with a corrected Avrami kinetics, has also been shown to provide a clear relationship between the transformation rate evolution and the velocity freeze-off. The transformation rate initiated by the Avrami kinetics evolves along the entire spinline and converges naturally to a low value at the take-up, consis-

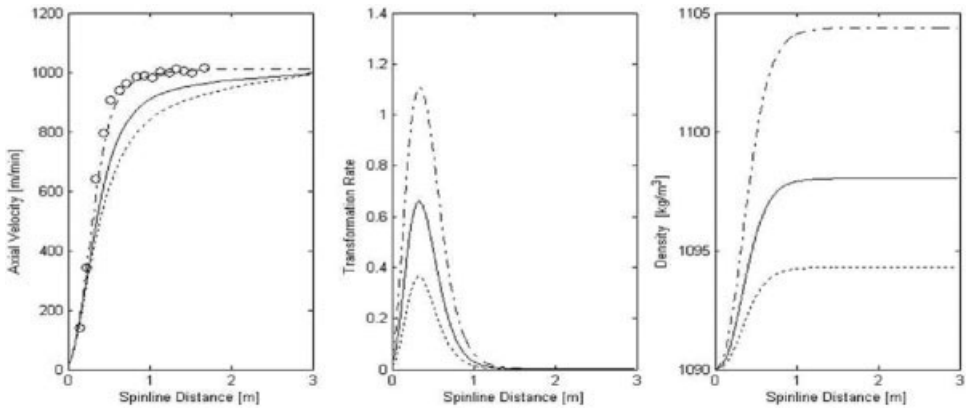

Figure 12 Effect of the Avrami parameter, K_{max}, on the prediction of velocity, transformation rate, and density (crystallinity) profiles for the Nylon 66 low-speed spinning run labeled S12 (data as circles). Predictions with a doubled K_{max} (dash-dotted lines) and a halved K_{max} (dotted lines) are compared with predictions (solid lines) using the value used for Nylon 66 in the present study.

tent with a near plateau in the transformation. The degree of transformation is shown to depend on the take-up speed, which is evidently the case in experiments.[16,17] Our results demonstrate that the maximum transformation rate attained along the spinline at high speeds corresponds with the freeze-off in velocity and orientation. On the other hand, at low speeds, the velocity and orientation never really freeze-off; rather they approach a plateau toward the end of the spinline due to the complete absence of FEC. Overall, we believe that the modified FEC model presented here can be applied to other polymer processes, such as film blowing and film casting, with appropriate changes in the algorithm based on the system of equations for those processes. As mentioned, we have recently shown that the modified integration algorithm in combination with use of the Pom-Pom model for the melt phase enables an excellent description of the spinning of PLA fibers.[15] The present model and algorithm are also more amenable for study of the dynamics of the full system of partial differential equations that describe the fiber-spinning process.[18]

NOMENCLATURE

o (subscript)	initial quantity ($z = 0$)
v_o	initial inlet velocity
A_o	initial flow area
$W_o = \rho v_o A_o$	mass throughput (constant)
G	polymer shear modulus (constant)
$z^* = z/L, \nabla^* = \nabla/L$	dimensionless distance from spinneret exit
$W^* = W_o/(\rho v_o A_o)$	dimensionless mass throughput
$v_z^* = v_z/v_o$	dimensionless axial velocity
$T^* = T/T_o$	dimensionless temperature
$c^* = cK/k_BT$	dimensionless conformation tensor
K	Elastic dumbbell spring constant
k_B	Boltzmann constant
$v^*_d = v_d/v_0$	dimensionless downward quench air velocity
$v^*_c = v_c/v_0$	dimensionless cross quench air velocity
$\tau^* = \tau/G$	dimensionless stress tensor
ρ	polymer density (constant)
μ_a	viscosity of quench air
s	surface tension (constant)
h	heat transfer coefficient
L	total length of spinline
C_p	specific heat
B	Bingham number
g	acceleration due to gravity (constant)
ΔH_f	latent heat of crystallization for polymer (constant)
ϕ_∞	ultimate degree of crystallinity (constant)
$D_1 = \dfrac{\rho v_o^2}{G}$	inertial forces (constant)
$D_2 = \dfrac{\pi \mu_a B L v_o}{G A_o}$	air drag $D_2(T^*, T^*_a, v^*_c, v^*_d, v^*, W^*)$
$D_3 = \dfrac{gL\rho}{G}$	gravity (constant)
$D_4 = \left(\dfrac{\pi s^2}{4A_oG^2}\right)^{1/2}$	surface tension (constant)
$D_5 = \left(\dfrac{4\pi L^2 h^2}{\rho^2 A_o C_p^2 v_o^2}\right)^{1/2}$	heat convection $D_5(T^*, T^*_a, v^*_c, v^*_d, v^*, W^*, x^*)$
$D_6 = G\rho C_p T_o$	viscous dissipation $D_6(x,T^*)$
$D_7 = \dfrac{\Delta H_f \phi_\infty}{C_p T_o}$	latent heat of crystallization $D_7(x,T^*)$
$T^*_a = \dfrac{T_a}{T_o}$	dimensionless air temperature

$T_r^* = \frac{T_r}{T_o}$ dimensionless reference temperature for shift factor

$T_m^* = \frac{T_m}{T_o}$ dimensionless melting temperature for shift factor

$Deb_o = \frac{v_o \lambda_a}{L}$ melt phase Deborah number

$Deb_a = (1 - x)^2 Deb_o$ scaled melt phase Deborah number ($Deb_a(x,T^*)$)

$Deb_{sc} = \frac{v_o \lambda_{sc}}{L}$ semicrystalline phase Deborah number ($Deb_{sc}(x,T^*)$)

$K^* = \frac{K_{av}^{1/n} L}{v_o}$ dimensionless Avrami rate temperature function $K^*(T^*)$

$a^* = \frac{a}{G}$ dimensionless stored free energy for elastic dumbbells

a' viscosity shift factor

Anthony J. McHugh acknowledges helpful discussions with Dr. A. K. Doufas concerning several interpretations of our results.

References

1. Doufas, A. K.; McHugh, A. J.; Miller, C. J Non-Newtonian Fluid Mech 2000, 92, 27.
2. Doufas, A. K.; McHugh, A. J.; Miller, C.; Immaneni, A. J Non-Newtonian Fluid Mech 2000, 92, 81.
3. Doufas, A. K.; McHugh, A. J. J Rheol 2001, 45, 403.
4. Doufas, A. K.; McHugh, A. J. J Rheol 2001, 45, 855.
5. Zieminski, K. F.; Spruiell, J. E. J Appl Polym Sci 1988, 35, 2223.
6. Patel, R. M.; Bheda, J. H.; Spruiell, J. E. J Appl Polym Sci 1991, 42, 1671.
7. Ziabicki, A. Fundamentals of Fiber Formation; Wiley-Interscience: New York, 1976.
8. E.I. DuPont de Nemours and Company, Private communication, 1999.
9. McHugh, A. J. J Appl Polym Sci 1975, 19, 125.
10. Marrucci, G. Trans Soc Rheol 1972, 16, 321.
11. Doufas, A. K.; Dairanieh, I. S.; McHugh, A. J. J Rheol 1999, 43, 85.
12. Vassilatos, G.; Knox, B. H.; Frankfort, H. R. E. In High Speed Fiber Spinning; Ziabicki, A., Kawai, H., Eds.; Krieger Publishing Co.: Malabar, 1991; p 383.
13. Suzuki, A.; Murata, H.; Kunugi, T. Polymer 1997, 39, 1351.
14. Haberkorn, H.; Hahn, K.; Breuer, H.; Dorrer, H.-D. J Appl Polym Sci 1993, 47, 1551.
15. Kohler, W. H.; Shrikhande, P.; McHugh, A. J. J Macromol Sci Phys 2005, 44, 185.
16. Perez, G. In High Speed Fiber Spinning; Ziabicki, A., Kawai, H. Eds.; Krieger Publishing Co.: Malabar, 1991; p 333.
17. Cakmak, M.; Kim, J. C. J Appl Polym Sci 1997, 61, 739.
18. Kohler, W. H., Ph.D. Thesis, unpublished results.